MDPI

Article

Magnetic Three-Dimensional Graphene: A Superior Adsorbent for Selective and Sensitive Determination of Nitrite in Water Samples by Ion-Pair Based-Surfactant-Assisted Solid-Phase Extraction Combined with Spectrophotometry

Mina Vasheghani Farahani [1], Sajad Karami [2], Hassan Sereshti [1,*] , Shokouh Mahpishanian [1], Somayeh Koupaei Malek [3] and Shahabaldin Rezania [4,*]

1 Department of Chemistry, Faculty of Science, University of Tehran, Tehran 14174, Iran; azonexkimia@gmqil.com (M.V.F.); sh.mahpishanian@gmail.com (S.M.)
2 Department of Nutrition, Dietetics and Food Sciences, Utah State University, Logan, UT 84322, USA; sajad.karami@usu.edu
3 Department of Chemistry, Universiti Teknologi Malaysia, Johor Bahru 81310, Johor, Malaysia; somaieh_kopaiee@yahoo.com
4 Department of Environment and Energy, Sejong University, Seoul 05006, Republic of Korea
* Correspondence: sereshti@ut.ac.ir (H.S.); shahab.rezania@sejong.ac.kr (S.R.)

Abstract: A straightforward, fast and efficient analytical method was developed which utilizes a magnetic composite called three-dimensional graphene (3D-G@Fe_3O_4) as an adsorbent to recover nitrite ions (NO_2^-) from environmental water samples. The investigation into the synthesized adsorbent contained an examination of its morphology, chemical composition, structural attributes, and magnetic properties. This comprehensive analysis was conducted using various instrumental techniques, including Fourier transform-infrared spectroscopy (FT-IR), scanning electron microscopy (SEM), Raman spectroscopy, X-ray diffraction (XRD), Brunauer-Emmett-Teller (BET), Barrett-Joyner-Halenda (BJH), and vibrating sample magnetometry (VSM). The adsorbent surface was activated by adding cetyltrimethylammonium bromide (CTAB) to the sample solution. To improve the selectivity and sensitivity of the method, nitrite ions were reacted with sulfanilic acid and chromotropic acid sequentially. An orange-red azo-dye complex was formed in the presence of nitrite ions with a clear absorbance peak at 514 nm. The effect of the main experimental parameters such as the pH of the sample solution, adsorbent dosage, and CTAB dosage was explored, and the optimization process was performed using a central composite design (CCD). The linear dynamic range (20–100 ng mL^{-1}) was determined under optimal experimental circumstances, yielding a reasonable determination coefficient (R2, 0.9993), a detection limit of 5.12 ng mL^{-1}, an enrichment factor of 167, and precision values of 1.0% intraday and 2.9% inter-day. The methodology successfully identified minute nitrite ions in environmental water samples with relative recoveries that varied between 96.05 and 101.6 ng mL^{-1}.

Keywords: nitrite ion; magnetic three-dimensional graphene; UV-vis spectrophotometry; central composite design; dispersive solid-phase extraction

1. Introduction

Nitrites are used in food preservation, soil fertilizers, detergents, wood pulp, dyes, and synthetic fibers. However, high concentrations of nitrite ions (NO_2^-) can affect human health [1,2]. A maximum contaminant level (MCL) of 11 mg L^{-1} for NO_2^- in drinking water has been set by the United States Environmental Protection Agency (US EPA) [3]. The escalating accumulation of NO_2^- in groundwater, rivers, and lakes has resulted in significant risks to both public health and the ecosystem [4]. Excessive amounts of NO_2^- in the human body can cause a health problem known as methemoglobinemia [5,6], and

also it has carcinogenic side effects due to the formation of N-nitrosamines [7]. Therefore, the determination of NO_2^- is very important for environmental and biological safety [8,9].

Because of the toxic nature of NO_2^-, the development of analytical methods for extraction and determination of traces of NO_2^- has gained special attention from various research groups in the world [10,11]. A variety of analytical techniques including capillary electrophoresis [12], ion chromatography [13], high-performance liquid chromatography (HPLC) [14,15], anodic voltammetry [16,17], spectrofluorimetry [18], square-wave voltammetry [19], and spectrophotometry [20], have been proposed for the determination of nitrite ions. Many of these methods are hindered by intricate and costly equipment and expensive reagents. However, spectrophotometry possesses several attractive features, including straightforward equipment, quick response time, satisfactory sensitivity and accuracy, and ease of use, while requiring minimal sample preparation [21–23]. However, before performing a trace analysis, sample preparation is a prerequisite. Various techniques, including solid-phase extraction (SPE) [24], cloud point extraction (CPE) [25–27], and liquid-phase microextraction (LPME) [28] have been developed for the extraction and preconcentration of nitrite ions. Among these methods, solid-phase extraction is probably the most widely applied technique, as it offers several advantages including operational simplicity, low solvent consumption, short processing time, possibility of process automation, and higher enrichment factor [29,30]. Indeed, the development of efficient adsorbents for solid-phase extraction (SPE) is an active area of research, and nanomaterials, especially carbon-based nanomaterials, have gained significant attention for their unique properties. Carbon-based nanomaterials offer advantages such as high specific surface area, chemical stability, and tunable surface functionalities, making them promising candidates for effective adsorption in SPE processes [31–33].

Graphene, a carbonaceous substance consisting of a single or a few layers of sp2-hybridized carbon atoms organized in a honeycomb structure, is commonly employed as a highly efficient adsorbent for various extraction processes [24]. Graphene, a 2D carbon allotrope, exhibits exceptional properties like high conductivity and surface area, rendering it promising for various applications. In contrast, 3D graphene encompasses structures with three-dimensional features, enhancing properties like surface area and mechanical stability. To discern between graphene and 3D graphene, diverse characterization techniques, including SEM, TEM, BET surface area analysis, pore size distribution measurements, and Raman spectroscopy are employed. These methods facilitate the visualization of morphology, quantification of surface area, and identification of structural differences, crucial for their distinct applications. In addition, many modification approaches have been used to improve its efficiency as an adsorbent. One of these appealing ways is producing three-dimensional graphene aerogel synthesized by the chemical vapor deposition method [34–36]. The unique properties of 3D graphene provide a high surface area, large mesoporous volume, and three-dimensional nano porous structure, which makes it a good candidate for employment as an efficient adsorbent for organic and inorganic species [37–40]. The scalable graphene-based sensors make them economically feasible for widespread deployment in various environmental monitoring and analytical settings. Additionally, the high sensitivity and selectivity of these sensors enable accurate detection and quantification of nitrite and nitrate ions in complex sample matrices. Moreover, the efficient response time of graphene-based sensors enhances the rapid analysis of water quality, facilitating timely decision-making and intervention measures in environmental management practices [41,42].

The primary aim of this paper is centered on devising a novel analytical method, which, while effective for detection purposes, may not be economically feasible for selective NO_2^- ions in water treatment or the removal of different pollutants from water samples [43,44]. Therefore, the emphasis of this study lies in advancing analytical methodologies rather than directly addressing the practical challenges associated with water treatment on a broad scale [45]. Therefore, the present study focuses on the utilization of an analytical technique to selectively recover and preconcentrate NO_2^- ions from low concentrations

in environmental water samples. Adding benzenoid chemicals and CTAB to the sample solution significantly enhanced the selectivity and sensitivity of the detection method. The proposed reagents exhibit a high degree of selectivity in their interaction with NO_2^-, hence mitigating the impact of coexisting interference ions exist in the environmental water samples.

The innovation of this study involves the utilization of magnetic three-dimensional graphene (3DG-Fe_3O_4) nanocomposite as a very efficient adsorbent for benzenoid chemicals, specifically CTAB (exchanged with NO_2^- ions), in the analysis of environmental water samples.

The adsorption process take place with π-π interaction followed by anion exchange between CTAB (Br^-) and NO_2^- ions. The objective of this study is to improve analytical methodologies by introducing magnetic adsorbent materials and employing a chromotropic method over the selective extraction of NO_2^- ions. The use of advanced magnetic adsorbents enhances the specificity of the method, ensuring that interference from other substances is minimized.

2. Experimental

2.1. Procedures and Materials

Ethanol (EtOH, 96%), acetone (>99%), acetonitrile (ACN, >99%), hydrochloric acid (HCl, 32%), dimethyl sulfoxide (DMSO, >99%), sodium chloride (NaCl, ≥99.5%), ferrous sulfate tetra hydrate ($FeSO_4 \cdot 4H_2O$), iron (III) chloride hexahydrate ($FeCl_3 \cdot 6H2O$, 99%), copper (II) nitrate trihydrate ($CuNO_3 \cdot 3H_2O$, 99.5%), mercury (II) chloride ($HgCl_2$), sodium nitrite ($NaNO_2$), ammonia (NH_3, 25%), disodium hydrogen phosphate (Na_2HPO_4) and sodium sulfate (Na_2SO_4) were acquired from Merck Chemicals in Darmstadt, Germany. Sigma Aldrich (St Louis, MO, USA) was the supplier of sodium nitrate ($NaNO_3$), methanol (MeOH, 99.8%), and cetyltrimethylammonium bromide (CTAB). The compound ammonium chloride (NH_4Cl) was acquired from Riedel-De Haen AG, a company based in Sleeze, Hanover, Germany. To prepare the NO_2^- stock solutions, 0.149 g of sodium nitrite were dissolved in 100 mL of distilled water and stored at a temperature of 4 °C until they were ready for use. On a daily basis, the operational medicines were prepared by gradually diluting the initial solution in distilled water.

2.2. Instrumentation

The absorption measurements were performed with a UV-2601 double-beam UV–vis spectrophotometer manufactured in Beijing, China. The spectrophotometer was coupled with a tungsten lamp serving as the light source. The measurements were conducted using a set of micro-cuvettes with an optical path length of 1 cm, manufactured by Fisher Scientific in Hampton, NH, USA. A WTW Inolab 720 pH meter from Weilheim, Germany was used to determine the pH measurements. The homogeneity of solutions was achieved through the utilization of a Eurosonic 4D ultrasonic water bath (Euronda, Montecchio Precalcino, Italy) and a ZX-Classic vortex mixer (Velp Scientifica, Milan, Italy). The infrared spectra in the range of 400 to 4000 cm^{-1} were recorded using the Equinox 55 FT-IR spectrometer, manufactured by Bruker in Bremen, Germany. The scanning electron microscopy (SEM) micrographs were captured using the Hitachi S-4160 machine, manufactured in Tokyo, Japan, running at a voltage of 5.0 kV. A vibrating sample magnetometer (VSM/AGFM Meghnatis Daghigh Kavir Co., Kashan, Iran) was employed to study the magnetic properties of the adsorbent at ambient temperature. The magnetic field intensity was systematically varied ranging from −10 to 10 kOe. The Cu K^3 radiation (κ = 1.54178 α) was used to acquire the X-ray diffraction (XRD) patterns using an X'Pert Pro MPD X-ray diffractometer at Almelo, The Netherlands.

The Raman spectra were obtained using a Senterra Dispersive Raman microscope (Bruker, Germany) that utilized a 785 nm wavelength laser for illumination. The Barrett-Joyner-Halenda (BJH) and Brunauer-Emmett-Teller (BET) methods were employed to determine the surface area, pore volume, and size analysis. These analyses were completed

using an ASAP 2000 Surface area and porosity analyzer manufactured by Micromeritics Instrument Corp., Norcross, GA, USA.

2.3. Preparation of the Adsorbent

Graphene oxide (GO) was initially synthesized using the Hummer method from graphite. Subsequently, 0.1 g of recently synthesized graphene oxide (GO) was added to 50 mL of distilled water and exposed to sonication for 15 min.

Subsequently, 0.7 g of ferrous sulfate ($FeSO_4$) was added to the solution, followed by an additional sonication period of 5 min. Then, the pH of the solution was adjusted to 11 using ammonia solution (NH_3, 25%). After that, the solution was placed in an oil bath at 90 °C for 6 h to formation of magnetic nanoparticles over GO. Next, the supernatant liquid was removed, and the sediment was washed three times with water and three times with EtOH. Afterward, the sediment was filtered and freeze-dried [46]. Finally, the freeze-dried powder was used as an adsorbent in the subsequent experiments.

2.4. The Procedure

First, 25 mL of the sample solution containing 40 ng mL^{-1} NO_2^- was placed in a screw cap vial, and then the pH of the solution was adjusted to 6.6 with 0.1 M HCl. After that, 40 mg of sulfanilic acid and 10 mg of chromotropic acid were added, respectively, to the solution, which is resulted the colored solution for spectroscopic determination purposes.

Next, 3 mg of CTAB was introduced into the solution and agitated for a period of 1 min to enhance the specific adsorption of NO_2^- ions. The solution was subjected to sonication for a duration of 1 min after the addition of 10 mg of the magnetic adsorbent. After the adsorption process, the adsorbent particles were separated from the solution by use of a magnet, and the aqueous supernatant was disposed of. Following that, 150 μL of dimethyl sulfoxide (DMSO) was added to the adsorbent, and the resulting mixture was mechanically stirred for 1 min. Then, the adsorbent was expelled from the solution once more by means of an external magnet, and the resultant organic supernatant was analyzed using a UV-vis spectrophotometer.

3. Results and Discussion

In this study, the crucial parameters influencing extraction recovery (*ER*) and enrichment factor (*EF*) were systematically examined and optimized through the implementation of a central composite design. After optimal conditions were obtained, the average *ER* and *EF* were calculated using the following equations:
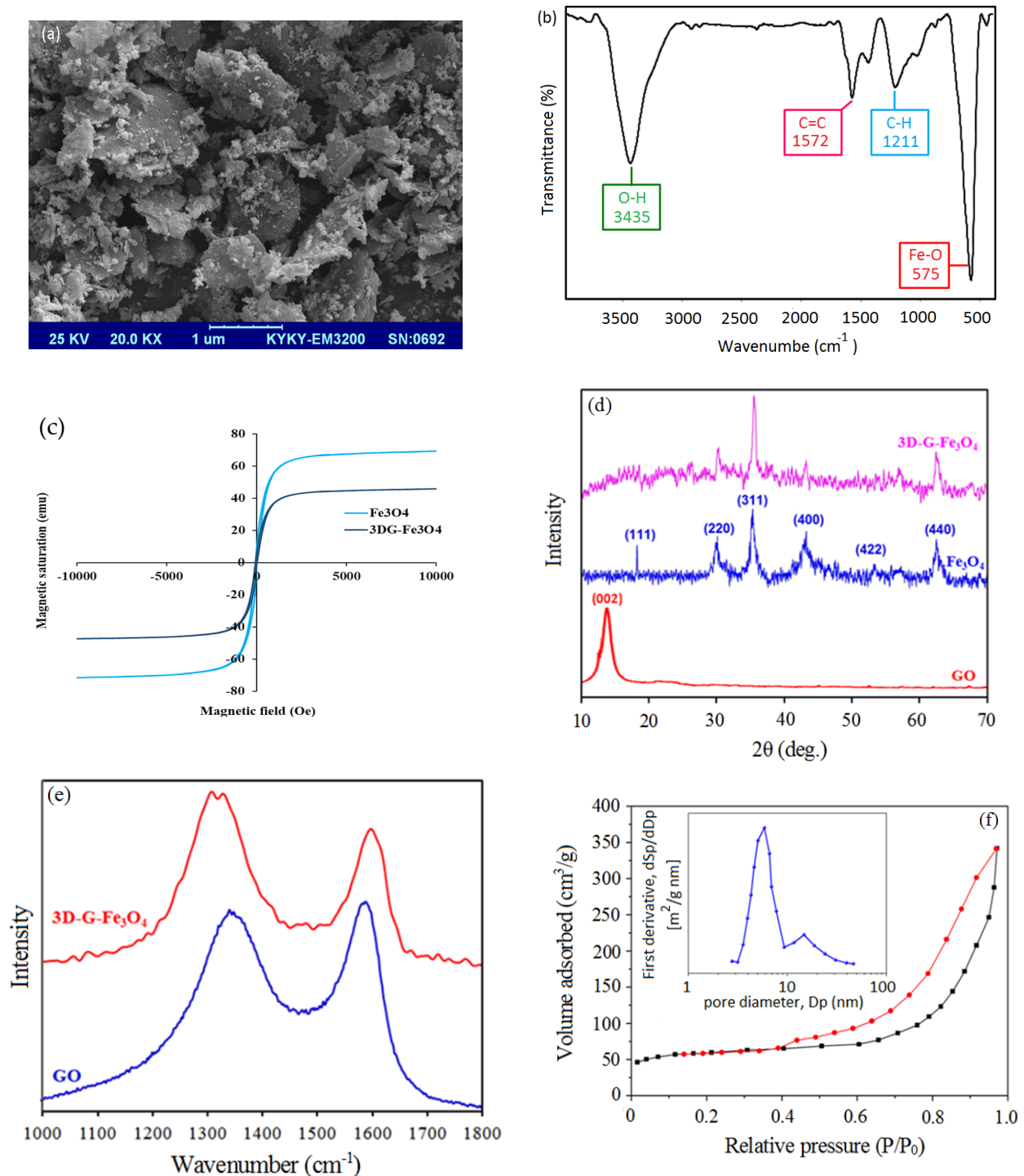
$$ER = \frac{C_f V_f}{C_i V_i} \times 100 \tag{1}$$

$$EF = \frac{V_i}{V_f} \tag{2}$$

In this context, the variable C_f is used to indicate the analyte concentration in the extraction solvent. C_i, on the other hand, specifies the starting concentration of the analyte in the sample solution. Additionally, V_i and V_f represent the volumes of the sample solution and the extraction solvent, respectively.

3.1. Characterization

The three-dimensional morphology of nano porous structure of 3D-G-Fe_3O_4 was investigated by scanning electron microscopy (Figure 1a). The SEM micrograph of 3D-G-Fe_3O_4 indicates that the iron oxide nanoparticles are well-distributed on the surface of the flake-like graphene sheets. The irregular standing of the graphene flakes-sheets over each other is the main characteristic of the three-dimensional architecture of 3D-G-Fe_3O_4. Figure 1b illustrates the FT-IR spectrum of 3D-G-Fe_3O_4. The peaks observed at 570, 1200, 1570, and 3400 cm^{-1} correspond to the stretching vibrations of Fe-O, –C-H, C=C, and

-OH, respectively. As can be seen, there is no peak at 1000 and 1750 cm^{-1} assigned to the characteristic epoxy and carbonyl stretching vibration bands that exist in the GO structure. This is due to the successful reduction of GO to G during synthesis of 3D-G@Fe$_3$O$_4$.

Figure 1. The characterization of the 3D-G-Fe$_3$O$_4$ nanocomposite by: (**a**) SEM micrograph of 3D-G-Fe$_3$O$_4$; (**b**) FT-IR spectrum of 3D-G-Fe$_3$O$_4$; (**c**) VSM magnetization curve of 3D-G-Fe$_3$O$_4$; (**d**) XRD pattern of the GO, Fe$_3$O$_4$ and 3D-G-Fe$_3$O$_4$; (**e**) the Raman spectra of graphene oxide (GO) and three-dimensional graphene-iron (3D-G-Fe$_3$O$_4$) are presented. (**f**) The nitrogen adsorption-desorption isotherms of three-dimensional graphene-iron (3D-G-Fe$_3$O$_4$) are shown in the inset, along with the BJH pore-size distributions.

A VSM was used to evaluate the magnetic characteristics of 3D-G-Fe$_3$O$_4$ under ambient conditions, incorporating field cycling. Figure 1c depicts a significant saturation magnetization value of 54.8 emu/g. This magnetic nanoparticle exhibits a lack of hysteresis, coercivity, and remanence. The recorded saturation magnetization values for 3DG-Fe$_3$O$_4$ were 39 emu/g. The results demonstrated the adsorbent's notable magnetic characteristics, indicating its potential for efficient separation by the application of an induced magnetic field.
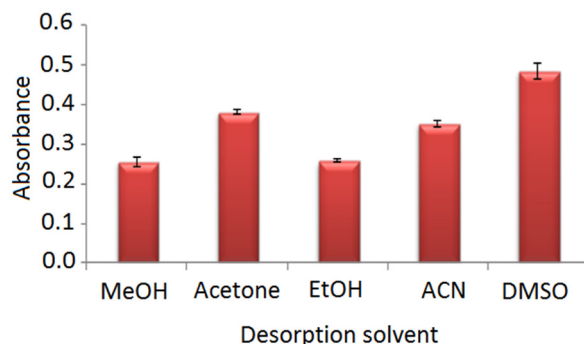
Figure 1d illustrates the X-ray diffraction (XRD) patterns of the GO, Fe$_3$O$_4$, and 3D-G-Fe$_3$O$_4$ samples. The XRD pattern of graphene oxide (GO) has a prominent peak at $2\iota = 12.26°$, which corresponds to the (0 0 2) reflection of GO. The observed diffraction peaks at 18° (111), 30° (220), 36° (311), 43° (400), 54° (422), and 64° (440) are consistent with the established X-ray diffraction (XRD) data of Fe3O4 nanoparticles, as reported in the standard spectrum of Fe$_3$O$_4$ (JCPDS, No. 65-3107). The final X-ray diffraction (XRD) pattern of the adsorbent is shown by the upper curve in Figure 1d. The distinct peak of GO has vanished, and the presence of Fe$_3$O$_4$ nanoparticles is apparent. These observed patterns indicate the synthesis of 3D-G-Fe$_3$O$_4$.

The Raman spectra of GO and 3D-G-Fe$_3$O$_4$ (Figure 1e) show the alterations in molecular organization caused by self-assembly and reduction, including the presence of disordered and imperfect structures. The graphene oxides (GO) spectra display two distinct peaks at around 1340 and 1590 cm^{-1}, aligning with the D and G bands, respectively. The D band is associated with modes that arise from structural defects and imperfections. On the other hand, the G band indicates the existence of carbon-carbon bonds that are sp2-hybridized. The ratio of ID intensity to IG intensity is as an indicator of abnormality. In GO, the ID/IG intensity ratio is 0.95, however in 3D-G-Fe$_3$O$_4$, it rises to 1.28. The observed rise in the ID/IG value suggests that the reduction and magnetization mechanisms have caused alterations in the GO structure, resulting in significant quantity of structural imperfections.

The specific surface area and pore size distribution of 3DG-Fe$_3$O$_4$ were measured using the BET and BJH procedures, respectively, as shown in Figure 1f. The hysteresis loop observed in the nitrogen adsorption-desorption isotherm falls within the relative pressure (p/p0) range of 0.45–0.95, indicating the existence of a porous structure. In a uniform pore system with a parallel wall slit-like pore structure, the adsorption behavior is marked by a notable increase in adsorption as the relative saturation pressure approaches, followed by a rapid decrease in desorption at the same pressure. The total specific surface area of pure 3DG-Fe$_3$O$_4$ was determined to be 218 m2 g^{-1} in the BET investigation. The BJH results demonstrated a narrow dispersion of pores inside the 3DG-Fe$_3$O$_4$ substance, exhibiting an average size of around 5.9 nm (Figure 1f).
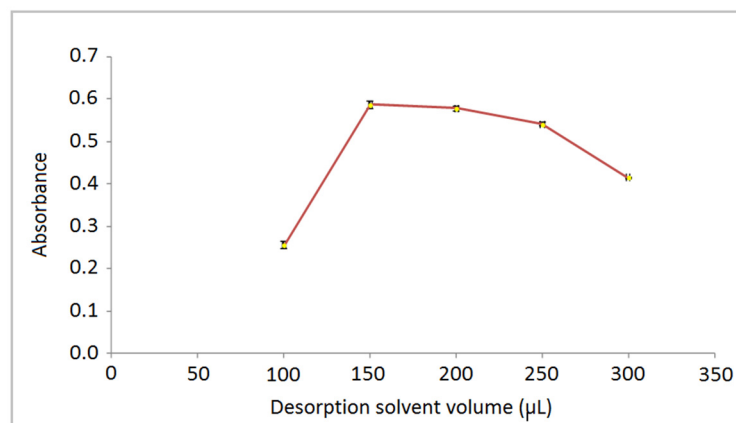
3.2. Effect of Desorption Solvents on Recovery

In adsorption experiments, it is necessary for the eluent to possess enough strength to completely extract the analyte from the adsorbent, while keeping the strongly attached interfering substances intact. The capacity of several solvents, such as acetone, methanol (MeOH), ethanol (EtOH), acetonitrile (ACN), and dimethyl sulfoxide (DMSO), to remove the analyte from the 3DG-Fe$_3$O$_4$ surface was evaluated using the suggested method. Figure 2 demonstrates that DMSO produced the most significant extraction recovery compared to the other solvents. This is probably due to some nature of DMSO, which is known for its high solvating power, that allows it to effectively solubilize and desorb polar and non-polar compounds from surfaces. In the case of nitrate ions, DMSO likely forms hydrogen bonds or other types of interactions with the polar nitrate ions, facilitating their desorption from the adsorbent surface. Although acetone and ACN also provided compatible recovery, DMSO is low in toxicity, stable and compatible with a variety of analytical techniques commonly used in chemistry and biochemistry, making it a versatile choice for desorption studies. Therefore, DMSO was selected as the desorption solvent for further studies.

Figure 2. Effect of types of solvent on recovery (Sample solution: 25 mL, 40 ng mL^{-1} NO$_2$).

The magnitude of the desorption solvent's volume is a crucial aspect in achieving dependable and consistent analytical outcomes. Thus, the influence of desorption solvent (DMSO) volume on the recovery of the analyte was investigated in the range of 100–300 µL. As shown in Figure 3, when DMSO volume was increased from 100 to 150 µL, the efficiency increased to a maximum at 150 µL, because as DMSO volume increased, more analyte desorbed from the adsorbent. Moreover, the efficiency decreased with volumes greater than 150 µL, since increasing the eluent volume led to the dilution. Hence, a volume of 150 µL was selected as the optimal volume of desorption solvent.

Figure 3. The influence of desorption solvent (DMSO) volume on the recovery of analyte. Sample solution: 25 mL, 40 ng mL^{-1} NO$_2$.

3.3. Optimization of the Procedure: A Central Composite Design

A rotatable and orthogonal central composite design (RO-CCD) was employed to optimize the essential factors and boost extraction efficiency. The utilization of a rotatable design guarantees uniform variability for every anticipated reaction, contingent exclusively on the distance from the central point of the design. Orthogonality allows for the independent evaluation of each factor, which enhances the reliability of the experimental design [47]. The Design-Expert 7.1.3 software package (Stat-Ease Inc., Minneapolis, MN, USA) was used to generate the experimental design and perform the related statistical analyses. After conducting initial studies, we identified three key elements that were found to be significant: the pH of the sample solution, the dosage of the adsorbent, and the amount of surfactant (CTAB). The number of experiments for the design was calculated using Equation (3) equal to 23.

$$N_{tot} = N_f + N_a + N_0 \tag{3}$$

In this given context, N_f denotes a full factorial design, which can be expressed as $N_f = 2f$, where f represents the number of factors. The symbol "N_a" represents a star-shaped

pattern with a factor of 2*f*, which helps in determining the curvature in the experimental area. In addition, N_0 represents the number of replicated trials conducted at the central point, where all parameters are set to their midway. Conducting the experiment at this central location allows for a reliable evaluation of experimental error. In the experimental area, the star points are deliberately positioned at angles of +± and—º with respect to the center. The equation determining the value of α, a crucial factor in ensuring rotatability, yields a value of ±1.682.

$$\alpha = \sqrt[4]{N_f} \tag{4}$$

To minimize the influence of uncontrolled factors, the tests were carried out in a randomized fashion. The tests were separated into two segments and completed over two consecutive days due to the impracticality of executing all experiments during a single working day. This methodology aimed to mitigate the potential inconsistencies arising from alterations implemented throughout the research.

The information shown in Table 1 provides a complete overview of the critical factors and their respective symbols and levels. This includes axial values (±±), factorial values (±1), and center points (0). Table S1 displays the data, which is located in the supplementary data file.

Table 1. The central composite design's factors and levels.

Factor	Symbol	Levels				
		−a [a]	−1	0 [b]	+1	+a [a]
pH	A	1.0	2.4	4.5	6.6	8.0
Adsorbent (mg)	B	5.0	10.0	17.5	24.9	30.0
CTAB [c] (mg)	C	1.0	2.8	5.5	8.2	10.0

[a] Axial points are equal to ±1.682 unit. [b] Central point. [c] Cetyl trimethylammonium bromide.

By applying multiple regression analysis to the design matrix, a fitted quadratic polynomial equation (model) was obtained. This model describes the relationship between the response and the independent parameters. It can be used to optimize the conditions and to predict the metrology data. The mathematical expression (Equation (5)) represents the response (absorbance) *Y* as a function of various factors *A*, *B*, and *C*, along with their interactions and quadratic terms. This predictive model in coded terms is presented in (Equation (5)).

$$Y = a_0 + a_1 A + a_2 B + a_3 C + a_4 AB + a_5 AC + a_6 A^2 + a_7 B^2 + a_8 C^2 \tag{5}$$

$a_0 = 0.53$; $a_1 = 0.05$; $a_2 = 0.06$; $a_3 = 0.03$; $a_4 = 0.03$; $a_5 = -0.03$; $a_6 = -0.08$; $a_7 = -0.02$; $a_8 = -0.07$. Y denotes the response (absorbance), the intercept is represented by a_0, and the coefficients of the model terms are denoted by the "*a*" terms (a_1 to a_8). The sign of each coefficient shows the direction of the correlation between the appropriate factor and the response. However, the coefficients' magnitudes might be used to indicate the significance of this correlation.

Subsequently, an analysis of variance (ANOVA) was conducted to assess the significance of the model terms. The analysis of variance (ANOVA) is a statistical procedure utilized to examine data obtained through an experimental design. Table 2 presents the quadratic model, including coded factors and statistical metrics such as F-value and *p*-value. The F-value, obtained by dividing the model mean square by the residual mean square, is a statistical test used to compare the variance of the model with the variance of the residuals (error).

Table 2. Analysis of variance (ANOVA) for response surface quadratic model.

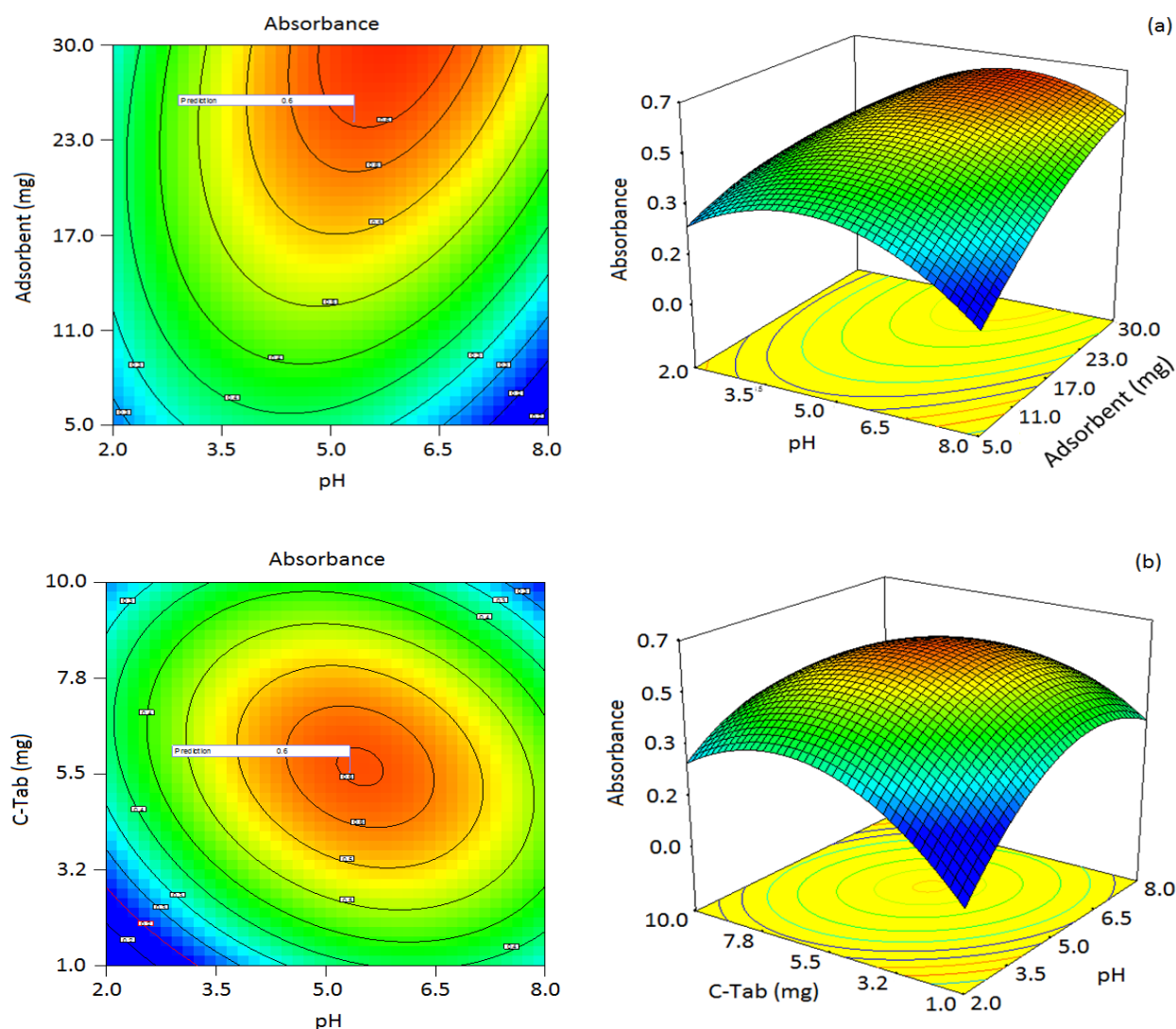| Source	Sum of Squares [a]	Df [b]	Mean Square [c]	F-Value [d]	*p*-Value [e] Prob > F	Significance
Block	1.2×10^{-3}	1	1.2×10^{-3}			
Model	0.3	8	0.037	21.12	<0.0001	Significant
A [f]	0.03	1	0.03	17.03	0.0012	
B [g]	0.051	1	0.051	28.67	0.0001	
C [h]	8.3×10^{-3}	1	8.3×10^{-3}	4.7	0.0493	
AB	8.6×10^{-3}	1	8.6×10^{-3}	4.87	0.0459	
AC	9.5×10^{-3}	1	9.5×10^{-3}	5.4	0.0369	
A^2	0.11	1	0.11	62.49	<0.0001	
B^2	7.0×10^{-3}	1	7.0×10^{-3}	4	0.0670	
C^2	0.076	1	0.076	43.07	<0.0001	
Residual [i]	0.023	13	1.8×10^{-3}			
Lack of Fit [j]	0.012	6	2.1×10^{-3}	1.38	0.3388	Not significant
Pure Error [k]	0.01	7	1.5×10^{-3}			
Cor total [l]	0.32	22				

[a] Sum of the squared differences between the average values and the overall mean. [b] Degrees of freedom. [c] Sum of squares divided by d.f. [d] Test for comparing term variance with residual (error) variance. [e] Probability of seeing the observed F-value if the null hypothesis is true. [f] pH. [g] Adsorbent dosage. [h] C-Tab (Cetrimonium bromide [$(C_{16}H_{33})N(CH_3)_3Br$]). [i] Consists of terms used to estimate experimental error. [j] Variation in the data around the fitted model. [k] Variation in the response in replicated design points. [l] Totals of all information corrected for the mean.

The ratio of model variances, as indicated by the model F-value, provides insight into the significance of the factors influencing the response. If the variances are approximately equal, the ratio will be close to one, suggesting that none of the factors significantly affect the response. In this case, the model F-value is 21.12, which implies that the model is statistically significant. The *p*-value associated with the F-value represents the probability of observing the given F-value under the assumption that the null hypothesis is true (meaning there is no significant factor effect). A small *p*-value suggests that the observed results are unlikely under the null hypothesis. Based on the model's statistically significant F-value, it can be inferred that at least one of the components has a significant impact on the response variable. Hence, a modest *p*-value would provide evidence to reject the null hypothesis, suggesting statistically significant factor effects inside the model. *p*-values below 0.05 indicate the significance of model terms, whereas values above 0.1 suggest their lack of significance. The model terms *A*, *B*, *C*, *AB*, *AC*, A^2, B^2, and C^2 hold statistical importance in the present scenario.

In Figure 4, three-dimensional (3D) response surfaces and contour plots are presented to illustrate the significant interactions, specifically the pH-adsorbent and pH-CTAB, in the context of the correlation between the response and these interacting factors. In these visualizations, the third factor is held constant at its center point. The utilization of this visual depiction facilitates the understanding of the intricate correlation between the reaction and the interaction of these particular components, providing a visual perspective on their influence on the total result [48]. Figure 4a shows the response surface and counterplots of the effect of pH-adsorbent dosage on the response in which the CTAB dosage was kept at 5.5 mg. As can be seen, the pH displays a quadratic effect on the response, so that when pH increased from 2 to 6, the response increased up to a maximum followed by a decline with its further increase. However, the adsorbent dosage shows an almost linear effect on the response with a maximum value of 30 mg.

In Figure 4b, the response surface and counter plots are depicted, specifically highlighting the influence of the pH-CTAB interaction on the response. Moreover, the zeta potential, a critical parameter characterizing surface charge, was investigated to elucidate the surface properties of the adsorbent material in this study [49,50]. The literature revealed a negative zeta potential at the zero-point charge (pH_{zpc}), indicating a net negative charge on the surface of the adsorbent particles under the experimental conditions [51]. This

negative charge is likely attributed to functional groups or ions present on the surface of the adsorbent material [52]. Zeta potential can significantly influence the adsorption behavior by affecting interactions with target species in the solution. Here, both CTAB and pH display quadratic effects on the response yielding maxima at 5.8 mg and 5, respectively. The CTAB surfactant acts as a bridge between the adsorbent and the sulfanilic acid-chronotropic acid. The pH level of the sample solution is a crucial factor that can influence the chemical structure of the analyte, the surface charge, and the binding sites of the adsorbent. The protonation/deprotonation reactions of the $3DG$-Fe_3O_4 surface OH groups at normal pH (~5.5–6.5) of the solution are in equilibrium, and thus the surface charge of the adsorbent is almost neutral. In this condition, CTAB acts as a linker between the adsorbent and analyte. It orients itself to the surface with its non-polar tail attached to the adsorbent and with its polar head toward the analyte. Therefore, as the amounts of both the adsorbent and surfactant increase, there is an augmentation in the availability of active sites for adsorption. This implies that higher quantities of the adsorbent and surfactant contribute to creating more sites on the material's surface, enhancing its capacity to adsorb substances.

Figure 4. (**a**) Three-dimensional (3D) response surface and counter plots the effect of pH-adsorbent dosage on the extraction recovery (the CTAB dosage was 5.5 mg); and (**b**) 3D response surface and counter plots of the effect of pH-CTAB dosage on the extract.

The numerical optimization function of the Design-Expert 7.1.3 program was utilized to determine the optimal operating conditions. Consequently, the objective for the impor-

tant variables was established as "within the specified range," and the response was set to "maximize". Hence, the most favorable parameters were determined to be a pH of 5.5, an adsorbent quantity of 25 mg, and a CTAB dosage of 5.7 mg, resulting in a calculated response of 0.59. To evaluate the precision of the outcomes projected by the response surface model, the approach was executed within the optimal parameters established by the model. Three replicates were used to measure the experimental response, resulting in a value of 0.57 with a relative standard deviation (RSD%) of 1.1%. A low relative standard deviation (RSD%) suggests high precision and consistency in the experimental measurements. In addition, the strong concurrence observed between the calculated and experimental responses (0.57) indicates that the response surface model forecasts the system's behavior within the specified optimum circumstances well.

3.4. Salt Effect

The impact of salt (NaCl) concentration on the method's efficiency was investigated within the range of 1–15% (*w/v*), employing the procedure outlined in Section 2.4. The results depicted in Figure S1 (supplementary data file) indicate that the concentration of salt did not have a statistically significant impact on the extraction of nitrite ions. This suggests that the method remains effective and consistent across the studied range of salt concentrations. The extraction of nitrite ions shows no significant sensitivity to variations in salt concentration within the specified range. The lack of significant influence of salt concentration on the extraction of nitrite ions could be attributed to factors such as the nature of ion pairing, solvation effects, adsorption competition, and electrostatic interactions involved in the extraction process. This is an advantage of this procedure for application in saline waters such as saline lakes, sea water and mineral natural waters.

3.5. Effect of Coexisting Ions

The influence of common coexisting ions in environmental water samples including NH_4^+, PO_4^{3-}, CO_3^{2-}, SO_4^{2-}, NO_3^-, Cl^-, Fe^{3+}, Hg^{2+}, Cu^{2+}, Na^+, and Ca^{2+} on the extraction of NO_2^- was also investigated under the optimal conditions. These ions in different concentrations were added individually to 25 mL of a solution containing 40 ng mL^{-1} of NO_2^- and the experiments were performed with the procedure described in Section 2.4. The tolerance limits of interfering ions in the analysis of NO_2^- ions were evaluated at concentrations that did not provide extraction recoveries below 90%. The results displayed in Table 3 demonstrate that these ions have a negligible impact on the extraction process's recovery at the measured concentration ratios. The approach exhibits resilience and specificity, as the existence of interfering ions at the designated concentrations does not have a negative impact on the retrieval of NO_2^- ions during the extraction procedure.

Table 3. Effect of coexisting ions on determination of NO_2^- (40 ng mL^{-1}).

Coexisting Ions	Coexisting Ion/NO_2^- Ratio (*w/w*)	ER
NH_4^+	1000	101
PO_4^{3-}	1000	98
CO_3^{2-}	1000	102
SO_4^{2-}	1000	97
NO_3^-	1000	99
Cl^-	1000	103
Fe^{3+}	1000	98
Hg^{2+}	1000	91
Cu^{2+}	1000	96
Na^+	1000	102
Ca^{2+}	1000	96

3.6. Adsorbent Reusability

The study examined the potential for reusing 3DG-Fe$_3$O$_4$ through consecutive adsorption and elution cycles. Following the extraction of the analyte from the sorbent, the adsorbent underwent two rounds of washing, initially with 2 mL of ethanol and subsequently with 2 mL of distilled water. Next, the adsorbent was subjected to a drying process and subsequently utilized for the succeeding cycle. The findings indicate that the utilization of 3DG-Fe$_3$O$_4$ can be repeated for at least 10 cycles without a significant decrease in extraction recovery. The extraction recoveries demonstrate the reusability and high performance of the adsorbent, which are consistently above 90% across various usages, as indicated in Table S2 (supplementary data file).

3.7. Analytical Method Validation

Method validation is essential for establishing the credibility, reliability, and fitness-for-purpose of analytical methods, ultimately contributing to the integrity and trustworthiness of analytical data generated in various applications. Hence, under the optimized conditions, which included a pH of 5.5, an adsorbent amount of 25 mg, and CTAB dosage of 5.7 mg, various performance parameters were evaluated. The limit of detection (LOD), limit of quantification (LOQ), linear dynamic range (LDR), precision, and enrichment factor were assessed. To establish the calibration curve, a series of standard solutions containing nitrite ions in the concentration range of 10–120 ng mL^{-1} were prepared. The method demonstrated linearity within the range of 20–100 ng mL^{-1}, with a determination coefficient (R2) of 0.9993, which was deemed quite satisfactory. The aforementioned findings indicate that the methodology demonstrates exceptional sensitivity and precision within the designated concentration range.

The enrichment factor, which is a measure of sensitivity enhancement, was calculated as the ratio of the slopes of the calibration graphs before and after preconcentration [53] and obtained equal to 167. The obtained values for LOD (CLOD = 3 Sd/m, where CLOD represents the limit of detection, Sd represents the standard deviation of the blank, and m represents the slope of the calibration graph) and LOQ (CLOQ = 10 Sd/m) were determined to be 5.12 ng mL^{-1} and 17.05 ng mL^{-1}, respectively, based on the given equations. The study focused on examining the intraday and inter-day precisions, measured as relative standard deviation (RSD), by evaluating a standard solution of nitrite ion (40 ng mL^{-1}). Three duplicates were conducted on the same day, while three replicates were acquired on different days using the proposed approach. The resulting RSD values were found to be 1.0% and 2.9%, respectively.

3.8. Real Samples

Testing real samples is crucial in the developed analytical method as it contributes to achieving accuracy and validating the method's recovery. Since accuracy based on recovery is essential for verifying the reliability and performance of analytical methods, identifying and mitigating sources of error or bias, and ensuring compliance with regulatory standards and quality assurance requirements. Hence, several real samples including tap water, sewage, mineral, and rain waters were selected, and developed MSPE was applied for the detection of NO$_2^-$. Following the collection of the samples, the next steps involved filtering them, adjusting their pH to the optimized value of 6.5, and subsequently subjecting them to testing in accordance with the proposed procedure under the established optimized conditions. This process ensures that the samples are appropriately prepared and treated to meet the specific requirements of the analytical method, enhancing the reliability and accuracy of the results obtained. To assess the matrix effect on the recovery efficiency of the method, different amounts of nitrite were spiked in the samples. The relative recoveries (*RR*) were computed using Equation (6) following the completion of the process, and the outcomes are presented in Table 4.

$$RR(\%) = \frac{C_{found} - C_{real}}{C_{added}} \times 100 \qquad (6)$$

Table 4. Extraction recovery for NO_2^- in environmental water samples.

Sample	Added (ng mL^{-1})	Found (ng mL^{-1})	RSD (%) (n = 3)	RR [a] (%)
Tap water [b]	-	-	-	-
	20	20.02	1.04	100.1
	80	81.28	1.1	101.6
Rain water [c]	-	-	-	-
	20	19.29	0.99	96.45
	80	78.36	1.03	97.95
Mineral water [d]	-	-	-	-
	20	19.84	1.06	99.2
	80	80.4	1.25	100.5
Sewage [e]	-	18.42	1	-
	20	37.63	0.97	96.05
	80	98.85	1.09	100.54
Sea water [f]	-	-	-	-
	20	19.57	0.96	97.85
	80	79.04	1.34	98.8

[a] Relative recovery. [b] The sample was collected from our lab. [c] The sample was collected from Tehran city (Tehran, Iran) during the autumn rain. [d] The sample was collected from a Dasani mineral water bottle. [e] The sample was collected from sewage of the university of Tehran's chemistry laboratories. [f] The water sample was collected from the Caspian sea.

The concentration of the analyte in the spiked sample solution, denoted as C found in the provided equation, is determined using the calibration curve. The term "C_{real}" represents the analyte concentration in the solution without any other substances added, whereas "C_{added}" refers to the concentration of the standard solution introduced into the actual sample.

The results indicate that the nitrite recoveries fall within the acceptable range of 96–102%. The results of this study suggest that the sample matrices used did not significantly impact extraction recoveries. Therefore, this methodology can be consistently utilized to quantify the nitrite concentration in water samples obtained from the surrounding environment, showcasing its reliability and suitability for real-world implementations.

3.9. Comparison with Similar Studies

The performance of the developed method was compared with other previously reported research for the determination of the nitrite and the results are summarized in Table 5. The extraction time is shorter than some of the other methods and comparable with the others. The volume of sample is smaller than the other methods. Furthermore, the enrichment factor surpasses that of the alternative approaches. Furthermore, the acceptable limit of detection (5.12 μg L^{-1}) is justified by the fact that the Environmental Protection Agency (EPA) has established a maximum contamination level (MCL) of 11 mg L^{-1} for nitrites in water.

Table 5. Comparison of the proposed method with other previously reported methods for the determination of NO_2^-.
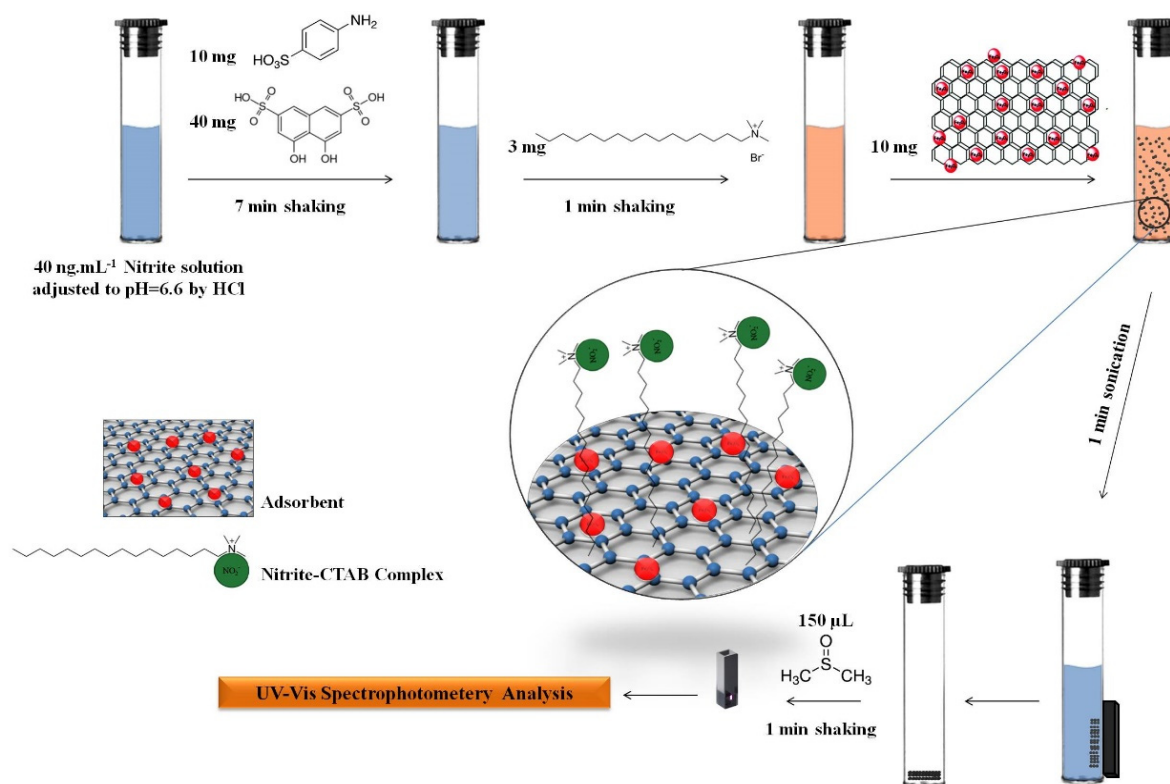
Analysis	Extraction	t (min)	V (mL) [a]	EF [b]	LOD [c]	LDR [d]	RSD (%)	R (%) [e]	Ref.
UV-Vis	SPE [f]	>36	250	125	3.1	10–550	<6.6	88–105	[9]
UV-Vis	LPE [g]	>60	-	-	60	500–6000	2.2	-	[20]
UV-Vis	-	>40	-	-	4.3	20–15000	<10	94–108	[54]
Fluorimetry	SPE [h]	1.5	160	160	0.034	0.1–80	0.6	94–102	[18]
Electrophoresis	-	2.5	-	-	0.82 [i]	-	0.99	89–104	[12]
UV-Vis	SPE [j]	10	25	167	5.12	20–100	1.01	93–110	This work

[a] Sample volume. [b] Enrichment factor. [c,d] ng mL^{-1}. [e] Recovery. [f] Solid-phase extraction with magnetic nanoparticles. [g] Liquid-phase extraction (aqueous two-phase system). [h] Dispersive magnetic SPE. [i] mmol L^{-1}. [j] SPE with 3D-G@Fe$_3$O$_4$.

3.10. Adsorption Mechanism

According to adsorption procedure scheme as shown in Figure 5, first the mixed solution of sulfanilic acid coupled with CTAB was absorbed on the surface of the graphene through π–π interaction and hydrophobic force interactives. In the next step, due to the anion exchange process between CTAB (Br$^-$) and nitrite ions (NO$_2^-$), the NO$_2^-$ ions selectively uptake over the magnetic adsorbent.

Figure 5. Proposed mechanism for selective adsorption of NO$_2^-$ ions over the magnetic graphene oxide.

4. Conclusions

The current investigation involved the synthesis of a magnetic three-dimensional graphene (3DG-Fe$_3$O$_4$) nanocomposite, which was subsequently employed as a highly efficient adsorbent for the purpose of selectively extracting and preconcentrating NO$_2^-$ in samples of ambient water.

The selectivity and sensitivity of detection were improved by using sulfanilic acid and chronotropic acid coupled with CTAB for visible detection by spectrophotometry. The reaction between the proposed reagents and NO$_2^-$ is almost selective and reduces the interferences from other ions which are usually present in environmental water samples. Furthermore, the substantial surface area and porosity exhibited by the 3D graphene oxide render it feasible to employ this methodology for saline materials, including seawater and those with intricate matrices. Moreover, the method offers several advantages such as good accuracy (recoveries 91.05–101.6%), high preconcentration factor (167), good precision (1.01%), low cost, selective, simple, and fast procedure. Furthermore, this method is considered environmentally friendly owing to its low organic solvent consumption with a small desorption solvent (150 μL). The study indicates that this environmentally friendly approach can effectively be employed for the determination of nitrite ions at low concentrations in real environmental samples. The combination of efficiency, low solvent usage, and applicability to low concentration levels enhances the method's sustainability and practical utility in environmental analyses.

References

1. Shakil, M.H.; Trisha, A.T.; Rahman, M.; Talukdar, S.; Kobun, R.; Huda, N.; Zzaman, W. Nitrites in Cured Meats, Health Risk Issues, Alternatives to Nitrites: A Review. *Foods* **2022**, *11*, 3355. [CrossRef] [PubMed]
2. Karwowska, M.; Kononiuk, A. Nitrates/Nitrites in Food-Risk for Nitrosative Stress and Benefits. *Antioxidants* **2020**, *9*, 241. [CrossRef] [PubMed]
3. Nolan, J.; Weber, K.A. Natural Uranium Contamination in Major U.S. Aquifers Linked to Nitrate. *Environ. Sci. Technol. Lett.* **2015**, *2*, 215–220. [CrossRef]
4. Della Betta, F.; Pereira, L.M.; Siqueira, M.A.; Valese, A.C.; Daguer, H.; Fett, R.; Vitali, L.; Costa, A.C.O. A sub-minute CZE method to determine nitrate and nitrite in meat products: An alternative for routine analysis. *Meat Sci.* **2016**, *119*, 62–68. [CrossRef]
5. Alagha, I.; Doman, G.; Aouthmany, S. SIMULATION 1 Methemoglobinemia Empty Line Calibri Size 12 Empty Line Calibri Size 12. *JETem* **2022**, *7*, S1–S26. [CrossRef]
6. Brender, J.D. Human Health Effects of Exposure to Nitrate, Nitrite, and Nitrogen Dioxide. In *Just Enough Nitrogen*; Springer International Publishing: Cham, Switzerland, 2020; pp. 283–294. [CrossRef]
7. Bryan, N.S. Inorganic Nitrate and Nitrite: Dietary Nutrients or Poisons? In *Nitrate Handbook*; CRC Press: Boca Raton, FL, USA, 2022; pp. 357–373.
8. Ackermann-Liebrich, U. Respiratory and Cardiovascular Effects of NO_2 in Epidemiological Studies. In *Encyclopedia of Environmental Health*; Elsevier: Amsterdam, The Netherlands, 2011; pp. 840–844. [CrossRef]
9. Tabrizi, A.B.; Sepehr, B. Extraction of ammonia and nitrite using modified magnetite iron oxide nanoparticles before spectrophotometric determination in different water samples. *Int. J. Environ. Anal. Chem.* **2015**, *95*, 833–846. [CrossRef]
10. Hetrick, E.M.; Schoenfisch, M.H. Analytical Chemistry of Nitric Oxide. *Annu. Rev. Anal. Chem.* **2009**, *2*, 409–433. [CrossRef]
11. Mahmud, M.A.P.; Ejeian, F.; Azadi, S.; Myers, M.; Pejcic, B.; Abbassi, R.; Razmjou, A.; Asadnia, M. Recent progress in sensing nitrate, nitrite, phosphate, and ammonium in aquatic environment. *Chemosphere* **2020**, *259*, 127492. [CrossRef]
12. Kalaycıoğlu, Z.; Erim, F.B. Simultaneous Determination of Nitrate and Nitrite in Fish Products with Improved Sensitivity by Sample Stacking-Capillary Electrophoresis. *Food Anal. Methods* **2015**, *9*, 706–711. [CrossRef]
13. Lopez-Moreno, C.; Perez, I.V.; Urbano, A.M. Development and validation of an ionic chromatography method for the determination of nitrate, nitrite and chloride in meat. *Food Chem.* **2016**, *194*, 687–694. [CrossRef]
14. He, L.; Zhang, K.; Wang, C.; Luo, X.; Zhang, S. Effective indirect enrichment and determination of nitrite ion in water and biological samples using ionic liquid-dispersive liquid–liquid microextraction combined with high-performance liquid chromatography. *J. Chromatogr. A* **2011**, *1218*, 3595–3600. [CrossRef] [PubMed]
15. Hewitt, D.; Alvarez, M.; Robinson, K.; Ji, J.; Wang, Y.J.; Kao, Y.H.; Zhang, T. Mixed-mode and reversed-phase liquid chromatography–tandem mass spectrometry methodologies to study composition and base hydrolysis of polysorbate 20 and 80. *J. Chromatogr. A* **2011**, *1218*, 2138–2145. [CrossRef] [PubMed]
16. Habib, I.H.I. Anodic Stripping Voltammetric Determination of Nitrite Using Carbon Paste Electrode Modified with Chitosan. *Am. J. Analyt Chem.* **2011**, *2*, 284–288. [CrossRef]
17. Alghamdi, A.H. Applications of stripping voltammetric techniques in food analysis. *Arab. J. Chem.* **2010**, *3*, 1–7. [CrossRef]
18. Tarigh, G.D.; Shemirani, F. Development of a selective and pH-independent method for the analysis of ultra trace amounts of nitrite in environmental water samples after dispersive magnetic solid phase extraction by spectrofluorimetry. *Talanta* **2014**, *128*, 354–359. [CrossRef] [PubMed]
19. Turdean, G.L.; Szabo, G. Nitrite detection in meat products samples by square-wave voltammetry at a new single walled carbon naonotubes–myoglobin modified electrode. *Food Chem.* **2015**, *179*, 325–330. [CrossRef]
20. Liu, Y.; Cai, Q.; Ma, W. Aqueous two-phase extraction and spectrophotometric determination of nitrite in food samples. *J. Appl. Spectrosc.* **2015**, *82*, 470–474. [CrossRef]

21. Abdelshakour, M.A.; Attala, K.; Elsonbaty, A.; Salam, R.A.A.; Hadad, G.M.; Mostafa, A.E.; Eissa, M.S. Eco-Friendly UV-Spectrophotometric Methods Employing Magnetic Nano-Composite Polymer for the Extraction and Analysis of Sexual Boosters in Adulterated Food Products: Application of Computer-Aided Design. *J. AOAC Int.* **2023**, *106*, 1608–1619. [CrossRef]

22. Markiewicz-Keszycka, M.; Cama-Moncunill, X.; Casado-Gavalda, M.P.; Dixit, Y.; Cama-Moncunill, R.; Cullen, P.J.; Sullivan, C. Laser-induced breakdown spectroscopy (LIBS) for food analysis: A review. *Trends Food Sci. Technol.* **2017**, *65*, 80–93. [CrossRef]

23. Lou, Y.; Xu, Q.; Chen, J.; Yang, S.; Zhu, Z.; Chen, D. Advancements in Sample Preparation Methods for the Chromatographic and Mass Spectrometric Determination of Zearalenone and Its Metabolites in Food: An Overview. *Foods* **2023**, *12*, 3558. [CrossRef]

24. Bianchi, F.; Sereshti, H.; Karimi, M.; Karami, S.; Mahpishanian, S.; Bidhendi, M.E.; Rezania, S.; Mojiri, A.; Kamyab, H.; Nodeh, H.R. Analysis of Polycyclic Aromatic Hydrocarbons Using Magnetic Three-Dimensional Graphene Solid-Phase Extraction Analysis of Polycyclic Aromatic Hydrocarbons Using Magnetic Three-Dimensional Graphene Solid-Phase Extraction Coupled with Gas Chromatography-Mass Spectrometry. *Separations* **2023**, *10*, 564. [CrossRef]

25. Ji, Y.; Wu, L.; Lv, R.; Wang, H.; Song, S.; Cao, M. Facile Cloud Point Extraction for the Separation and Determination of Phenolic Acids from Dandelion. *ACS Omega* **2021**, *6*, 13508–13515. [CrossRef]

26. Pocurull, E.; Fontanals, N.; Calull, M.; Aguilar, C. Environmental Applications. In *Liquid-Phase Extraction*; Elsevier: Amsterdam, The Netherlands, 2020; pp. 591–641. [CrossRef]

27. Hussain, C.M.; Keçili, R. Sampling and Sample preparation techniques for environmental analysis. In *Modern Environmental Analysis Techniques for Pollutants*; Elsevier: Amsterdam, The Netherlands, 2020; pp. 75–119. [CrossRef]

28. Sereshti, H.; Abdolhosseini, G.; Soltani, S.; Sadatfaraji, H.; Karami, S.; Nodeh, H.R. A green ternary polymeric deep eutectic solvent used in dispersive liquid-liquid microextraction technique for isolation of multiclass pesticides in fruit juice samples. *J. Food Compos. Anal.* **2023**, *124*, 105663. [CrossRef]

29. Badawy, M.E.I.; El-Nouby, M.A.M.; Kimani, P.K.; Lee; Lim, W.; Entsar; Rabea, I. A review of the modern principles and applications of solid-phase extraction techniques in chromatographic analysis. *Anal. Sci.* **2022**, *38*, 1457–1487. [CrossRef]

30. Rosendo, L.M.; Brinca, A.T.; Pires, B.; Catarro, G.; Rosado, T.; Guiné, R.P.F.; Araújo, A.R.T.S.; Anjos, O.; Gallardo, E. Miniaturized Solid Phase Extraction Techniques Applied to Natural Products. *Processes* **2023**, *11*, 243. [CrossRef]

31. Liu, W.-X.; Song, S.; Ye, M.-L.; Zhu, Y.; Zhao, Y.-G.; Lu, Y. Nanomaterials with Excellent Adsorption Characteristics for Sample Pretreatment: A Review. *Nanomaterials* **2022**, *12*, 1845. [CrossRef]

32. Zhang, B.T.; Zheng, X.; Li, H.F.; Lin, J.M. Application of carbon-based nanomaterials in sample preparation: A review. *Anal. Chim. Acta* **2013**, *784*, 1–17. [CrossRef]

33. Liu, J.; Li, R.; Yang, B. Carbon Dots: A New Type of Carbon-Based Nanomaterial with Wide Applications. *ACS Central Sci.* **2020**, *6*, 2179–2195. [CrossRef] [PubMed]

34. Jayaramulu, K.; Mukherjee, S.; Morales, D.M.; Dubal, D.P.; Nanjundan, A.K.; Schneemann, A.; Masa, J.; Kment, S.; Schuhmann, W.; Otyepka, M.; et al. Graphene-Based Metal−Organic Framework Hybrids for Applications in Catalysis, Environmental, and Energy Technologies. *Chem. Rev.* **2022**, *122*, 17241–17338. [CrossRef]

35. Ehrmann, C.; Li, N.; Abbas, Q.; Shinde, P.A.; Abdelkareem, M.A.; Alami, A.H.; Mirzaeian, M.; Yadav, A.; Olabi, A.G. Materials Graphene Synthesis Techniques and Environmental Applications. *Materials* **2022**, *15*, 7804. [CrossRef]

36. Jiang, L.; Liu, Y.; Zeng, G.; Liu, S.; Hu, X.; Zhou, L.; Tan, X.; Liu, N.; Li, M.; Wen, J. Adsorption of estrogen contaminants (17β-estradiol and 17α-ethynylestradiol) by graphene nanosheets from water: Effects of graphene characteristics and solution chemistry. *Chem. Eng. J.* **2018**, *339*, 296–302. [CrossRef]

37. Yang, Z.; Zhou, S.; Feng, X.; Wang, N.; Ola, O.; Zhu, Y. Recent Progress in Multifunctional Graphene-Based Nanocomposites for Photocatalysis and Electrocatalysis Application. *Nanomaterials* **2023**, *13*, 2028. [CrossRef] [PubMed]

38. Ma, Y.; Chen, Y. Three-dimensional graphene networks: Synthesis, properties and applications. *Natl. Sci. Rev.* **2015**, *2*, 40–53. [CrossRef]

39. Asghari, Z.; Sereshti, H.; Soltani, S.; Taghizadeh, M.; Karami, S.; Bidhendi, M.E.; Rezania, S. An alginate-based eutectogel impregnated with polyvinylpyrrolidone/benzoic acid deep eutectic solvent and magnetic carboxylated multiwalled carbon nanotubes: Evaluated as sorbent in green microextraction of pesticides. *J. Chromatogr. B* **2023**, *1229*, 123865. [CrossRef] [PubMed]

40. To, J.W.F.; Chen, Z.; Yao, H.; He, J.; Kim, K.; Chou, H.-H.; Pan, L.; Wilcox, J.; Cui, Y.; Bao, Z. Ultrahigh Surface Area Three-Dimensional Porous Graphitic Carbon from Conjugated Polymeric Molecular Framework. *ACS Cent. Sci.* **2015**, *1*, 68–76. [CrossRef] [PubMed]

41. Li, D.; Wang, T.; Li, Z.; Xu, X.; Wang, C.; Duan, Y. Application of Graphene-Based Materials for Detection of Nitrate and Nitrite in Water—A Review. *Sensors* **2019**, *20*, 54. [CrossRef]

42. Marlinda, A.R.; An'amt, M.N.; Yusoff, N.; Sagadevan, S.; Wahab, Y.A.; Johan, M.R. Recent progress in nitrates and nitrites sensor with graphene-based nanocomposites as electrocatalysts. *Trends Environ. Anal. Chem.* **2022**, *34*, e00162. [CrossRef]

43. Ifa, L.; Syarif, T.; Sartia, S.; Juliani, J.; Nurdjannah, N.; Kusuma, H.S. Techno-economics of coconut coir bioadsorbent utilization on free fatty acid level reduction in crude palm oil. *Heliyon* **2022**, *8*, e09146. [CrossRef] [PubMed]

44. Ifa, L.; Yani, S.; Nurjannah, N.; Darnengsih, D.; Rusnaenah, A.; Mel, M.; Mahfud, M.; Kusuma, H.S. Techno-economic analysis of bio-briquette from cashew nut shell waste. *Heliyon* **2020**, *6*, e05009. [CrossRef]

45. Kusuma, H.S.; Izzah, D.N.; Linggajati, I.W.L. Microwave-assisted drying of Ocimum sanctum leaves: Analysis of moisture content, drying kinetic model, and techno-economics. *Appl. Food Res.* **2023**, *3*, 100337. [CrossRef]

46. Cong, H.-P.; Ren, X.-C.; Wang, P.; Yu, S.-H. Macroscopic Multifunctional Graphene-Based Hydrogels and Aerogels by a Metal Ion Induced Self-Assembly Process. *ACS Nano* **2012**, *6*, 2693–2703. [CrossRef] [PubMed]

47. Collins, L.M.; Dziak, J.J.; Li, R. Design of Experiments with Multiple Independent Variables: A Resource Management Perspective on Complete and Reduced Factorial Designs. *Psychol. Methods* **2009**, *14*, 202–224. [CrossRef] [PubMed]

48. Sereshti, H.; Karimi, M.; Samadi, S. Application of response surface method for optimization of dispersive liquid–liquid microextraction of water-soluble components of *Rosa damascena Mill.* essential oil. *J. Chromatogr. A* **2009**, *1216*, 198–204. [CrossRef] [PubMed]

49. Morales-Benítez, I.; Montoro-Leal, P.; García-Mesa, J.C.; Verdeja-Galán, J.; Alonso, E.I.V. Magnetic graphene oxide as a valuable material for the speciation of trace elements. *TrAC Trends Anal. Chem.* **2022**, *157*, 116777. [CrossRef]

50. Hosseini, N.M.; Sheshmani, S.; Ashraf; Shahvelayati, S.; Ahmadi, R.; Adhami, F. Development and Characterization of Environmentally-Friendly Magnetically Graphene Oxide-Embedded Chitosan as a Recyclable Heterogeneous Photocatalyst. *J. Polym. Environ.* **2023**, *32*, 1952–1971. [CrossRef]

51. Hardiansyah, A.; Yang, M.-C.; Liao, H.-L.; Cheng, Y.-W.; Destyorini, F.; Irmawati, Y.; Liu, C.-M.; Yung, M.-C.; Hsu, C.-C.; Liu, T.-Y. Magnetic Graphene-Based Sheets for Bacteria Capture and Destruction Using a High-Frequency Magnetic Field. *Nanomaterials* **2020**, *10*, 674. [CrossRef] [PubMed]

52. Mccoy, T.M.; Brown, P.; Eastoe, J.; Tabor, R.F. Noncovalent Magnetic Control and Reversible Recovery of Graphene Oxide Using Iron Oxide and Magnetic Surfactants. *ACS Appl. Mater. Interfaces* **2015**, *7*, 2124–2133. [CrossRef] [PubMed]

53. Gürkan, R.; Altunay, N.; Gürkan, N. Extraction, preconcentration and spectrophotometric determination of trace levels of thiosulfate in environmental waters. *J. Iran. Chem. Soc.* **2017**, *14*, 1033–1049. [CrossRef]

54. Shariati-Rad, M.; Irandoust, M.; Mohammadi, S. Spectrophotometric determination of nitrite in soil and water using cefixime and central composite design. *Spectrochim. Acta A Mol. Biomol. Spectrosc.* **2015**, *149*, 190–195. [CrossRef]